Mapping the human lateral geniculate nucleus and its cytoarchitectonic subdivisions using quantitative MRI ☆

Christa Müller-Axt [a,b,*], Cornelius Eichner [b], Henriette Rusch [c], Louise Kauffmann [b,d], Pierre-Louis Bazin [b,e], Alfred Anwander [b], Markus Morawski [b,c], Katharina von Kriegstein [a]

[a] Faculty of Psychology, Technical University of Dresden, Dresden 01069, Germany
[b] Max Planck Institute for Human Cognitive and Brain Sciences, Leipzig 04103, Germany
[c] Paul Flechsig Institute of Brain Research, University of Leipzig, Leipzig 04103, Germany
[d] LPNC, Grenoble Alpes University, Grenoble 38000, France
[e] Integrative Model-Based Cognitive Neuroscience Research Unit, Department of Psychology, University of Amsterdam, Amsterdam 1001 NK, The Netherlands

ARTICLE INFO

ABSTRACT

The human lateral geniculate nucleus (LGN) of the visual thalamus is a key subcortical processing site for visual information analysis. Due to its small size and deep location within the brain, a non-invasive characterization of the LGN and its microstructurally distinct magnocellular (M) and parvocellular (P) subdivisions in humans is challenging. Here, we investigated whether structural quantitative MRI (qMRI) methods that are sensitive to underlying microstructural tissue features enable MR-based mapping of human LGN M and P subdivisions. We employed high-resolution 7 Tesla *in-vivo* qMRI in $N = 27$ participants and ultra-high resolution 7 Tesla qMRI of a *post-mortem* human LGN specimen. We found that a quantitative assessment of the LGN and its subdivisions is possible based on microstructure-informed qMRI contrast alone. In both the *in-vivo* and *post-mortem* qMRI data, we identified two components of shorter and longer longitudinal relaxation time (T_1) within the LGN that coincided with the known anatomical locations of a dorsal P and a ventral M subdivision, respectively. Through ground-truth histological validation, we further showed that the microstructural MRI contrast within the LGN pertains to cyto- and myeloarchitectonic tissue differences between its subdivisions. These differences were based on cell and myelin density, but not on iron content. Our qMRI-based mapping strategy paves the way for an in-depth understanding of LGN function and microstructure in humans. It further enables investigations into the selective contributions of LGN subdivisions to human behavior in health and disease.

1. Introduction

The human sensory thalami are central processing sites for the analysis of sensory information. A growing body of empirical evidence suggests that to-date we are only starting to understand the function of these nuclei and their subdivisions for human behavior and cognition in health (Saalmann and Kastner, 2011) and disease (Dorph-Petersen et al., 2009; Livingstone et al., 1991; Yücel et al., 2003).

The human lateral geniculate nucleus (LGN) of the visual thalamus consists of six distinct neuronal layers, two ventral magnocellular (M) layers, four dorsal parvocellular (P) layers, and intercalated koniocellular (K) layers (Andrews et al., 1997). Much of our current knowledge about the LGN stems from invasive non-human primate studies (Nassi and Callaway, 2009). This is partly due to the fact that investigations of the LGN and its main neuronal layers (coined M and P subdi-

visions) in humans *in-vivo* face considerable technical challenges. First, the LGN's small size and deep location within the brain makes it difficult to map the LGN using non-invasive MRI (Forstmann et al., 2016). Second, conventional image resolutions in *in-vivo* MR examinations are likely insufficient to fully disentangle distinct signal contributions of M and P subdivisions due to partial volume effects (Weibull et al., 2008). Third, any microstructural tissue differences between LGN subdivisions (i.e., subcortical gray matter) can be assumed to result in only subtle differences in MR contrast.

Resolving LGN subdivisions in humans *in-vivo* would, however, be of keen interest to gain a better understanding of their contribution to a variety of cognitive processes such as visual perception, selective attention and visual awareness (Denison and Silver, 2012; Livingstone and Hubel, 1988; Schneider and Kastner, 2009); their functional interactions and structural connectivity with the cerebral cortex (Callaway, 2005);

---

and their role in human disorders such as glaucoma (Gupta et al., 2006; Zhang et al., 2016), multiple sclerosis (Evangelou et al., 2001; Thurtell et al., 2009), developmental dyslexia (Livingstone et al., 1991; Müller-Axt et al., 2017; Stein, 1997), autism spectrum- (Milne et al., 2002) and mood disorders (Dorph-Petersen et al., 2009). Indeed, most clinical research on the integrity of the LGN and its subdivisions in humans is based on *post-mortem* studies, which generally lack the opportunity to relate structure to function and often suffer from small sample sizes (Livingstone et al., 1991). They, however, also give first indications that LGN subdivisions can be selectively impaired.

Recent advances in high-field structural MRI have enabled measurements at unprecedented spatial resolutions. Especially the introduction of quantitative MRI (qMRI) methods provides access to high-quality imaging data, which allow the assessment of biophysical tissue parameters that reflect the underlying microstructure (van der Zwaag et al., 2016). Quantitative MR parameters, such as the longitudinal relaxation time T_1, provide insights into tissue myelination (Geyer et al., 2011; Lutti et al., 2014; Stüber et al., 2014) and allow tissue segmentation based on cyto- and myeloarchitecture (Bazin et al., 2014; Kuehn et al., 2017; Waehnert et al., 2016). To our knowledge, no study has yet attempted to resolve LGN subdivisions *in-vivo* based on microstructure-informed qMRI. However, such an approach seems promising as M and P layers differ markedly in cyto- and myeloarchitecture: M neurons are characterized by large cell bodies and are more sparsely distributed relative to the smaller, densely packed P neurons (Andrews et al., 1997; Hassler, 1966). In addition, M neurons have thicker and more myelinated nerve fibers compared to the thinner, less myelinated axons of P neurons (Hassler, 1966; Merigan and Maunsell, 1993; Yoonessi and Yoonessi, 2011). Mapping strategies based on qMRI could also provide an alternative approach to previous EPI-based functional MRI (fMRI) strategies (Denison et al., 2014; Zhang et al., 2016, 2015) to circumvent typical technical shortcomings associated with fMRI. These include limited image resolution, blurring, geometric distortions, and lengthy acquisition times (Bernstein et al., 2004). Here, we utilized recent technological advances in high-field structural qMRI and addressed whether microstructure-informed MR contrasts enable MR-based mapping of human LGN subdivisions.

The study involved three steps: (i) *in-vivo* high-resolution 7 Tesla qMRI assessment of $N = 27$ bilateral LGNs (500 μm isotropic), (ii) ultra-high resolution 7 Tesla qMRI of a *post-mortem* human LGN specimen (220 μm isotropic), and (iii) histology of the same LGN specimen. We expected that microstructural tissue differences between LGN subdivisions are reflected in T_1 relaxation and that this subdivisional T_1 contrast is driven by local differences in myelin density between M and P layers. As myelin density and T_1 relaxation are inversely related (Geyer et al., 2011; Stüber et al., 2014), a key question is which cyto- and myeloarchitectonic features of the LGN primarily constitute myelin density and, thus, T_1 contrast between LGN subdivisions. First, higher axonal myelination of M than P neurons (Beaton, 2004; Stein, 2002; Yoonessi and Yoonessi, 2011) might result in an increased myelin density, and consequently, shorter T_1 relaxation of the M relative to the P subdivision. Alternatively, the overall sparser distribution of M neurons (Andrews et al., 1997; Nassi and Callaway, 2009) might decrease myelin density and translate into increased T_1 relaxation of the M relative to the P subdivision. A lower myelin density in M layers as opposed to P layers has been previously observed in marmoset monkeys (Pistorio et al., 2006).

We first aimed to address whether qMRI can guide the differentiation of LGN subdivisions in humans *in-vivo*. In a next step, we assessed *in-vivo* quantitative T_1 contrasts between LGN subdivisions using ultra-high resolution qMRI of an independent *post-mortem* LGN tissue sample to compare it to histology. This served to discern between microstructural sources underlying subdivisional LGN T_1 contrast. The *in-vivo* qMRI data were used to create a detailed population atlas of the LGN and its M and P subdivisions, which we have made publicly available.

2. Methods

2.1. In-vivo MRI

2.1.1. Participants

To address whether qMRI can guide the differentiation of LGN subdivisions *in-vivo,* we analyzed high-resolution structural qMRI data from $N = 27$ (15 females, 12 males) healthy participants with a mean age of 26.5 ± 3.8 years. We opted for a large publicly available repository of *in-vivo* qMRI datasets with excellent image resolution. To the best of our knowledge, the employed repository is the largest open access source of high-resolution and quantitative MR brain imaging data (Tardif et al., 2016) (available for download at http://openscience.cbs.mpg.de/bazin/7T_Quantitative/). Of the $N = 28$ available datasets in the repository, the dataset of one participant was omitted due to a diagnosis of developmental dyslexia. All participants, except for one, were right-handed as assessed with the Edinburgh Inventory (Oldfield, 1971), and none had a prior history of neurological or psychiatric disorders. Written informed consent was obtained from all participants. The study was approved by the ethics committee of the Medical Faculty, University of Leipzig, Germany (Approval # 177–2007).

#### 2.1.2. High-resolution 7T quantitative MRI data acquisition

High-resolution structural qMRI data were acquired on a 7 Tesla Magnetom MRI system (Siemens Healthineers, Erlangen, Germany) using a 24-channel head array coil (NOVA Medical, Wilmington MA, USA). Each hemisphere was imaged separately using a 3D-MP2RAGE sequence (Marques et al., 2010) with the following imaging parameters: 500 μm isotropic resolution, TE = 2.45 ms, TR = 5000 ms, TI_1 / TI_2 = 900 / 2750 ms, α_1 / α_2 = 5 / 3°, FoV = 224 × 224 × 104 mm^3, and Partial Fourier (PF) of 6/8 in slice direction. Participants were awake and instructed to lie still and relax during the image acquisition. The MRI acquisition took approximately 28 mins per hemisphere. The 3D-MP2RAGE sequence included two readouts at different inversion times, from which a quantitative T_1 (qT_1) map was estimated. A single whole-brain qT_1 map of the two hemispheres was created by co-registering both images and interpolating the result at 400 μm isotropic resolution using a rigid (6-parameter) transformation. Finally, the qT_1 maps of all participants were skull-stripped (Bazin et al., 2014). All processing was performed using CBS Tools (https://www.nitrc.org/projects/cbs-tools/).

2.1.3. LGN segmentations on in-vivo quantitative T_1 maps

Bilateral LGNs were defined through manual segmentation by two independent raters on the $N = 27$ high-resolution *in-vivo* qT_1 maps following a standardized procedure (SI Methods) in FSLView (https://fsl.fmrib.ox.ac.uk/fsl/fslwiki/FslView). Dice coefficients were computed to assess inter-rater reliability (Dice, 1945). The obtained coefficients yield a measure of agreement between raters and range from 0 (no agreement) to 1 (perfect agreement). The LGN segmentations of both raters were merged to create an LGN mask for each participant and each hemisphere. For the LGN masks, only those voxels that were segmented by both raters were considered.

2.1.4. In-vivo LGN subdivisions

For the identification of *in-vivo* LGN subdivisions, we first normalized the LGN masks of all participants into a common reference space. This was done by computing a study-specific qT_1 group template from the $N = 27$ *in-vivo* high-resolution qT_1 maps using symmetric normalization (SyN) in ANTs (Avants et al., 2008) (SI Methods and Fig. S1a–c). SyN is a state-of-the-art registration algorithm that globally minimizes registration parametrization and is unbiased towards any individual input image in template generation (Avants et al., 2010). The obtained SyN registration parameters were applied to the individual qT_1 maps, followed by averaging of all registered maps, to create the study-specific
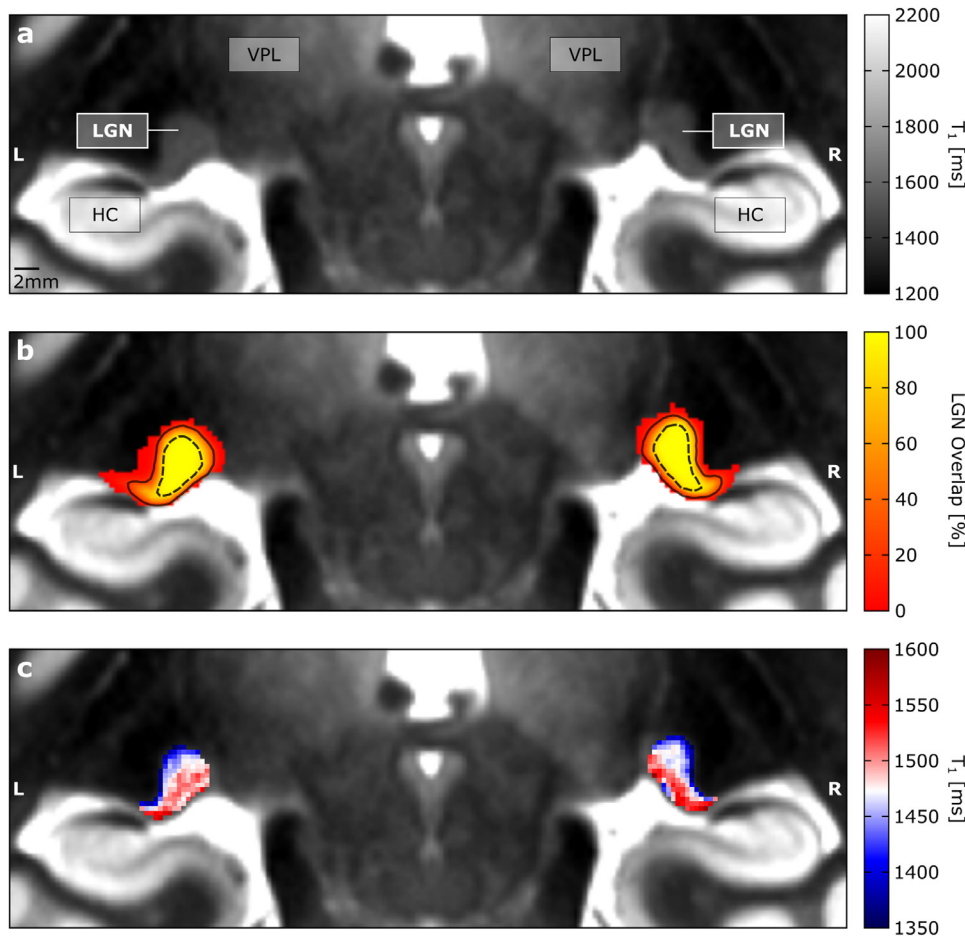
Fig. 1. Coronal view of the study-specific qT_1 group template along with the bilateral *in-vivo* LGN population atlas. Displayed voxel dimensions correspond to 0.4 mm isotropic image resolution. (a) The figure shows a coronal slice of the study-specific qT_1 group template, centered on the lateral geniculate nuclei. Anatomical labels are provided for spatial orientation and comparison to Fig. 3g: LGN = lateral geniculate nucleus, HC = hippocampus, VPL = ventral posterior lateral thalamic nucleus and other thalamic nuclei. (b) Study-specific qT_1 group template as shown in panel (a), overlaid with the left and right LGN population atlas. Color coding indicates the overlap in LGN location across the $N = 27$ participants. The bilateral LGN population atlas is shown at full extent, i.e., with no threshold applied. Overlaid black contours depict the atlas set to thresholds of at least 20% (solid lines) and 90% (dashed lines) overlap across participants. (c) Study-specific qT_1 group template as shown in panel (a) with an adapted color map within the LGN to highlight the range of LGN qT_1 values. On visual inspection, shorter qT_1 values (blue) coincide with the anatomical location of a dorsal P subdivision, whereas longer qT_1 values (red) coincide with a ventral M subdivision. The range of LGN qT_1 values is shown for voxels of the probabilistic LGN atlas (panel b) with at least 50% overlap across subjects. (For interpretation of the references to color in this figure legend, the reader is referred to the web version of this article.)

qT_1 group template (SI Methods, Figs. 1a and S1c). The respective registration parameters were also applied to the individual LGN masks, which were combined for each hemisphere to create a bilateral LGN population atlas in a common reference (i.e., template) space (SI Methods and Fig. 1b). The value of each voxel in the bilateral LGN population atlas corresponds to the percentage of the population (i.e., of the $N = 27$ participants) that contained that voxel in their respective registered individual LGN mask. The LGN population atlas was carefully validated (SI Methods).

In a next step, the LGN population atlas was set to a threshold of at least 50% overlap across participants, and subsequently intersected with the registered single-subject qT_1 maps (in template space) to extract the underlying qT_1 values of the left and right LGN for each participant. We used the LGN population atlas (at a population threshold of $\geq$ 50%) rather than the participant-specific LGN masks to extract the underlying LGN qT_1 distributions to ensure that the subsequent subdivision analyses were based on LGN voxels that were shared in at least 50% of participants. *In-vivo* LGN subdivisions were identified by means of individual Gaussian mixture models. A mixture model, D, with two Gaussian components, G, each representing one of the LGNs main subdivisions, was fit to each participant's left- and right-hemispheric qT_1 distribution:

$$D(A_1, \mu_1, A_2, \mu_2, \sigma) = A_1 \, G(\mu_1, \sigma) + A_2 \, G(\mu_2, \sigma)$$

Here, the variables A_i, μ_i, σ refer to the amplitude, mean and standard deviation of a Gaussian distribution, G. Model fitting was performed using the 'curve_fit' function in SciPy (Virtanen et al., 2020). The following anatomically motivated boundary conditions were employed on the Gaussian mixture models: (i) the volume of the Gaussian P-component is at least 50% of the total qT_1 distribution, which relates to prior anatomical findings in human *post-mortem* studies that the

P subdivision occupies a larger part of total LGN volume than the M subdivision (Andrews et al., 1997); (ii) the Gaussian P-component and the Gaussian M-component are centered between the 5th and the 50th percentile and between the 50th and 95th percentile of the total qT_1 distribution, respectively. This boundary condition relates to the observed *in-vivo* contrast with shorter T_1 relaxation in dorsolateral parts of the LGN (see Fig. 1c).

To estimate separability between subdivisions given model D, we introduced a separability index, ϑ, based on the subdivisional distribution parameters:

$$\vartheta = \frac{|\mu_1 - \mu_2|}{\sigma}$$

LGN subdivisions were judged to be separable for model fits with $\vartheta \geq 1$. This threshold for ϑ was estimated from Monte Carlo simulations on model, D (SI Methods; Fig. S2).

For model fits with separable subdivisions ($\vartheta \geq 1$), each of the two individual Gaussian fits (i.e., M and P components) was normalized by the envelope of the summed Gaussian components (i.e., whole distribution of $M + P$ components). This was done for each LGN separately, resulting in M and P distribution probabilities per individual LGN. The distribution probabilities were then interpolated using the SciPy function 'interp1d' to compute continuous transfer functions between qT_1 intensities and distribution probabilities. Each transfer function was subsequently applied to each respective individual *in-vivo* LGN qT_1 map to compute voxel-wise M and P distribution probability maps.

For non-separable distributions with $\vartheta < 1$, model fits were discarded, and binary thresholding was applied assuming an 80/20 volume allocation between magnocellular and parvocellular subdivisions as known from classic anatomical studies (Andrews et al., 1997).

In a final step, the M and P distribution probability maps were combined for each hemisphere across participants to create bilateral population atlases of LGN M and P subdivisions.

2.1.5. Statistical analyses

Hemispheric differences between *in-vivo* qMRI LGN volumes and qT_1 values were assessed through two-sided paired t-tests. Correlations between left- and right-hemispheric LGN volumes and qT_1 values were assessed using two-sided Pearson's correlations. For all statistical tests, the significance level α was defined at 5% ($p \leq 0.05$). Statistical analyses were performed in MATLAB R2019b (version 9.7, MathWorks, MA, USA; https://www.mathworks.com/products/matlab.html).

2.2. Post-mortem MRI and histology

2.2.1. Collection and preparation of post-mortem human brain tissue

A human *post-mortem* brain sample was provided by the former Brain Banking Centre Leipzig of the German Brain-Net, operated by the Paul Flechsig Institute of Brain Research, Medical Faculty, University of Leipzig. The brain sample consisted of a left hemisphere of a female patient (89 years, cause of death myocardial infarction, tissue fixation 24 h *post-mortem*). Neuropathological assessment revealed no signs of any neurological diseases. The entire procedure of case recruitment, acquisition of the patient's personal data, protocols and informed consent forms, performing the autopsy, and handling the autopsy material has been approved by the responsible authorities (GZ 01GI9999–01GI0299; Approval # 82–02). Following standard Brain Bank procedures, the block was immersion-fixed in 3% paraformaldehyde and 1% glutaraldehyde in phosphate-buffered saline (PBS; pH 7.4) for at least six weeks. The tissue block was cut to approximately $30 \times 15 \times 30$ mm (left-right, posterior-anterior, superior-inferior dimension, respectively) in size and included the LGN and part of the hippocampus. To prepare the sample for high-resolution qMRI, the LGN specimen was placed in an acrylic sphere of 60 mm diameter filled with perfluoropolyether (PFPE; Fomblin©, Solvay Solexis Inc., Bollate, Italy). PFPE is a synthetic oil that does not generate any MR signal. Its application, therefore, has the specific advantage that the measured *post-mortem* qMR parameters are not affected by partial volume effects of other signal-generating substances (Iglesias et al., 2018) adjacent to the analyzed tissue.

2.2.2. Quantitative MRI data acquisition and reconstruction

For the qMRI acquisition of the LGN specimen, we employed a multi-contrast steady-state approach. The basic principle of this method is to acquire 3D FLASH MR data with different contrasts, which are subsequently fit to an MR signal model (Helms et al., 2008). As a result, quantitative maps are obtained for T_1 and proton density (PD).

Ultra-high resolution *post-mortem* MRI data were acquired on a 7T Magnetom MRI system (Siemens Healthineers, Erlangen, Germany) using a custom-built Helmholtz coil (Müller et al., 2019). FLASH data were acquired using the following imaging parameters: 220 μm isotropic resolution, TE = 4.0 – 40.7 ms (12 echo times), TR = 95 ms, FoV = $50 \times 50 \times 24.64$ mm^3, BW = 343 Hz/Px, slab-selective RF excitation, no GRAPPA, and PF = 8/8. Three MR contrasts were obtained by variation of the excitation flip angle (α): a PD-weighted (PDw) contrast at $\alpha_{PD} = 17°$, a high-signal Ernst angle contrast at $\alpha_{Ernst} = 36°$, and a T_1-weighted (T_1w) contrast at $\alpha_{T1} = 82°$. The acquisition of each MR contrast took approximately 43 mins. Throughout the MR acquisition, the temperature of the LGN specimen was monitored and ranged from 37.5 to 38.8 °C.

Quantitative MR parameters were calculated from the MR imaging data in a two-stage procedure using Python (Virtanen et al., 2020). First, the echo times of all contrasts were evaluated jointly to determine voxel-wise values for T_2^*. All FLASH contrasts were then extrapolated to TE = 0 ms to remove T_2^* contrast contamination (Weiskopf et al., 2014). In a second step, the extrapolated data of all flip angles were fit voxel-wise to the steady-state Ernst-equation (Helms et al., 2008) to calcu-

late quantitative maps of T_1 and PD. To remove potential impacts from smooth, low frequency field inhomogeneity, the two quantitative maps were bias-field corrected using N4 inhomogeneity correction in ANTs (Tustison et al., 2010). Any bias-field correction of the absolute qMRI data might affect the quantitative nature of the data. For this reason, no conclusions can be drawn about absolute qMRI values but only about relative qMRI differences between LGN subdivisions. Also note that *post-mortem* qMRI data are characterized by systematically reduced relaxation times due to tissue fixation and rehydration processes (Shatil et al., 2018), which make absolute comparisons with *in-vivo* relaxation parameters challenging. Comparisons between modalities should therefore be based on relative qMRI contrasts only (e.g., by comparing relative T_1 relaxation time differences between LGN subdivisions between *in-vivo* versus *post-mortem* qMRI data).

2.2.3. LGN segmentation on post-mortem quantitative T_1 map

The LGN was defined on the bias-field corrected ultra-high resolution qT_1 map of the *post-mortem* qMRI acquisition through manual segmentation by two independent raters in FSLView. We used the qT_1 map for segmentation, as this map provides excellent gray-white matter contrast and therefore allows for better visualization and improved segmentation of deep gray matter structures such as the LGN (Marques et al., 2010; Marques and Gruetter, 2013; Müller-Axt et al., 2017). Windowing parameters for the manual segmentation were chosen to maximize LGN contrast and were identical for both raters. Inter-rater reliability for the manual LGN segmentation was assessed by means of a Dice coefficient (Dice, 1945). Segmentations of both raters were conjoined to only include those voxels that were segmented by both raters into the LGN mask. The LGN mask was used in subsequent analyses of *post-mortem* LGN subdivisions.

2.2.4. LGN subdivisions in post-mortem tissue

For the identification of *post-mortem* LGN subdivisions, we extracted the distribution of qT_1 values within the LGN mask. The extracted LGN qT_1 distribution was first cleaned from outliers by removing the 0.1% smallest and 0.1% largest qT_1 values. Subsequently, the Gaussian mixture model, D, was fit to the cleaned distribution using the SciPy function 'curve_fit' (Virtanen et al., 2020), as was done for the *in-vivo* qMRI data. Given the high resolution and signal-to-noise ratio of the *post-mortem* qMRI data, the model fit was performed without any boundary conditions. Next, each of the two individual Gaussian fits (i.e., M and P components) was normalized by the envelope of the summed Gaussian components (i.e., whole distribution of $M + P$ components) to transfer LGN qT_1 intensities into distribution-based probabilities. The distribution probabilities were then interpolated using the SciPy function 'interp1d' to compute a continuous M and P transfer function between qT_1 intensities and distribution probabilities. In a final step, the M and P transfer functions were applied to the ultra-high resolution *post-mortem* LGN qT_1 map to compute voxel-wise M and P distribution probability maps.

2.2.5. Histology

To validate and explain qT_1 contrasts between LGN subdivisions, the *post-mortem* LGN sample was subjected to microstructural histology. We included three commonly employed types of markers that covered the main microstructural properties contributing to qT_1 contrast (Stüber et al., 2014): these included immunohistochemical staining with anti-human neuronal protein C/D (anti-HuC/D) and myelin basic protein (anti-MBP) for marking cell bodies and myelin, respectively. In addition, histochemical staining with Perls' Prussian blue (PB) as a marker for ferric iron was included as another potential source of qT_1 contrast (Stüber et al., 2014). Detailed procedures for immunohistochemical staining with HuC/D and MBP as well as histochemical staining with PB are described in the supplementary materials (SI Methods).

Following (immuno-)histochemical staining, histological LGN layers were traced and labeled (SI Methods) to enable layer-specific cell density

(anti-HuC/D) and optical density analyses of myelin (anti-MBP) and iron content (PB). Measures of cell density and optical density were extracted for each of the two fused dorsal P layers (i.e., layers P3/5 and P4/6) and each of the two ventral M layers of the posterior LGN (SI Methods), given previous reports of higher morphological and inter-individual consistency in laminar arrangements compared to the anterior LGN.

3. Results

3.1. Identification of LGN subdivisions by in-vivo MRI

LGNs of each hemisphere were segmented based on the $N = 27$ *in-vivo* qT_1 maps. Inter-rater reliability measures of the LGN segmentations indicated high agreement between the two raters (mean Dice coefficients: left LGN = 0.88 ± 0.02; right LGN = 0.89 ± 0.02). The segmentation procedure resulted in mean LGN volumes of 113.5 ± 13.3 mm^3 and 120.9 ± 14.0 mm^3 for the left and right LGN, respectively. LGN volumes were significantly correlated across hemispheres ($R = 0.73$, $p = 2.2 \times 10^{-5}$), and were significantly greater in the right than in the left hemisphere ($t(26) = 3.9$, $p = 0.7 \times 10^{-3}$). Underlying mean qT_1 values of the left and right LGN masks showed a high correspondence (left LGN: 1469.9 ± 61.2 ms, right LGN: 1469.2 ± 60.9 ms; $R = 0.93$, $p = 3.8 \times 10^{-12}$), and did not significantly differ from each other ($t(26) = 0.16$, $p = 0.88$). A normalization of the LGN masks to the study-specific qT_1 group template (Figs. 1a and S1c), followed by overlaying of the masks for each hemisphere, resulted in a bilateral LGN population atlas that showed a strong correspondence across participants with the underlying anatomy (Fig. 1a, b). Visual inspection of the study-specific qT_1 template revealed higher T_1 values in ventral parts of the LGN and lower T_1 values in dorsal parts of the nucleus (Fig. 1c). On visual inspection, the observed T_1 contrast within the LGN coincided with the known anatomical locations of a ventral M and a dorsal P subdivision. The bilateral LGN population atlas (Fig. 1b), set to a threshold of at least 50% overlap across participants (Fig. 2a, b), was subsequently employed to extract the individual LGN qT_1 distributions of all participants in each hemisphere. For the identification of *in-vivo* LGN subdivisions, two-component Gaussian mixture models (see Methods, section '*In-vivo* LGN subdivisions') were fit to the extracted single-subject LGN qT_1 distributions, and the resulting segmentation of the subdivisions were combined across participants for each hemisphere. The resulting population maps of the P and M subdivisions revealed a similar pattern as observed on the study-specific qT_1 template: P-classified voxels with shorter T_1 relaxation showed the largest overlap across participants in dorsal parts of the LGN (Fig. 2c, d), whereas M-classified voxels with longer T_1 relaxation showed the largest overlap in ventral parts of the nucleus (Fig. 2e, f). Thresholding of these P and M subdivision populations maps to at least 50% overlap across participants revealed two spatially distinct, non-overlapping clusters, which in turn coincided with the expected anatomical location of a dorsal P and a ventral M LGN subdivision (Fig. 2g, h). The P and M subdivision population maps in Fig. 2c–h show the combined single-subject segmentations including those for which the mixture model fit detected separable LGN subdivisions ($\vartheta \geq 1$; Left: $n = 14$, Right: $n = 18$; Fig. S3) and those for which we used binary 80/20 thresholding (Andrews et al., 1997) ($\vartheta < 1$; Left: $n = 13$, Right: $n = 9$) (see Methods, section '*In-vivo LGN subdivisions*'). The ratio of the sums of the successfully identified P and M components across participants resulted in average contributions of 84.7 ± 13.8% (P-component) versus 15.3 ± 13.8% (M-component) to total LGN volume in the left hemisphere; and 85.4 ± 12.0% (P-component) versus 14.6 ± 12.0% (M-component) in the right hemisphere.
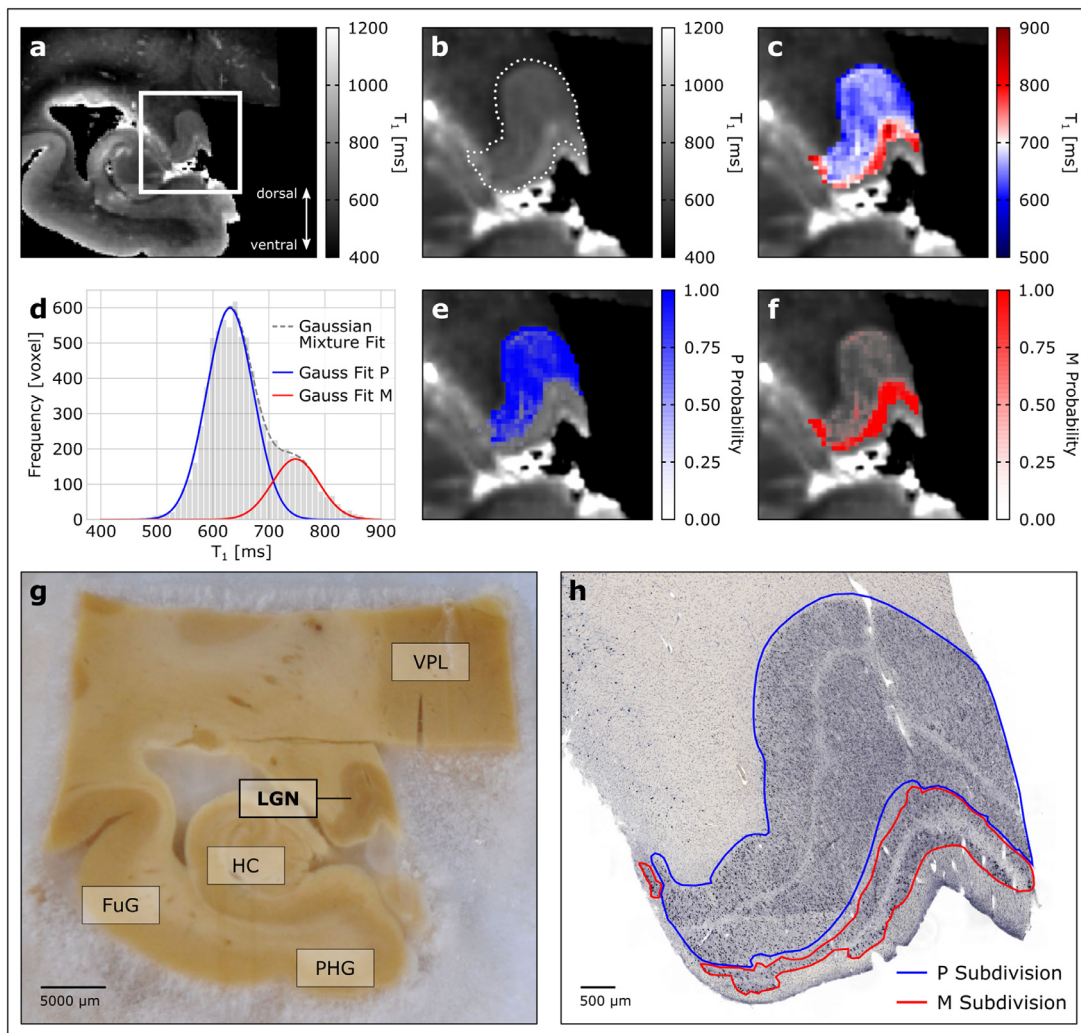
3.2. Identification of LGN subdivisions by post-mortem MRI

We next assessed the qT_1 map of the *post-mortem* tissue sample. There was a clear contrast in qT_1 between the LGN and surrounding gray and white matter structures (Fig. 3a). LGN segmentations of the two raters
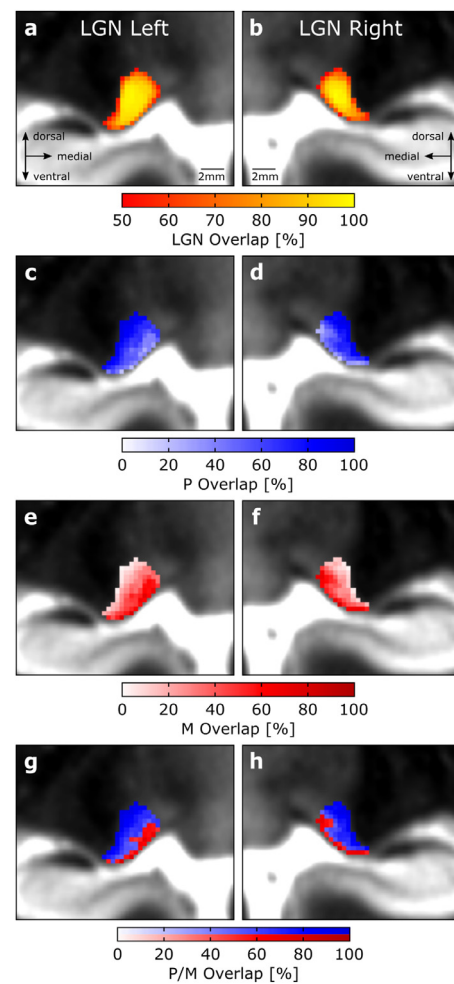
Fig. 2. *In-vivo* LGN subdivisions overlaid on a slice of the study-specific qT_1 group template in coronal view. Displayed voxel dimensions correspond to 0.4 mm isotropic image resolution. (a, b) Zoomed view of the left (a) and right (b) LGN population atlas based on $N = 27$ participants, set to a threshold of at least 50% overlap across participants. (c-d) Zoomed view of the population atlas of the left (c) and right (d) LGN P subdivision based on $N = 27$ participants. Color coding indicates the overlap in P-classified voxels across participants. (e, f) Zoomed view of the population atlas of the left (e) and right (f) LGN M subdivision based on $N = 27$ participants. Color coding indicates the overlap in M-classified voxels across participants. (g, h) Zoomed view of the left (g) and right (h) LGN P and M subdivision population maps, set to a threshold of at least 50% overlap across participants. A threshold of 50% overlap enabled a voxel-wise assignment to either the P or M subdivision given the same probability range for both subdivisions. The blue-shaded part of the color bar indicates the overlap for the dorsal P subdivision, while the red-shaded part of the color bar indicates the overlap for the ventral M subdivision. (For interpretation of the references to color in this figure legend, the reader is referred to the web version of this article.)

on the qT_1 map were in excellent agreement (Dice coefficient 0.95) and resulted in an LGN volume of 87.6 mm^3. Similar as for the *in-vivo* qT_1 data, visual inspection of the qT_1 map also revealed a clear contrast within the LGN: longer T_1 relaxation coincided with the expected anatomical location of a ventral M subdivision, while shorter T_1 relaxation coincided with a dorsal P subdivision (Fig. 3b, c). Fitting a Gaussian mixture model with two components to the underlying distribution of qT_1 values in the LGN mask (see Methods, section '*LGN subdivisions in post-mortem tissue*') revealed one component centered around shorter qT_1 values, and another component centered around longer qT_1 values (Fig. 3d). A subsequent normalization of these two individual Gaussian

Fig. 3. Identification of LGN subdivisions on ultra-high resolution qMRI and histological validation in a left-hemispheric tissue sample. (a) Coronal slice of the *post-mortem* qT$_1$ map of the tissue sample. The white rectangle marks the location of the LGN. (b) Zoomed view of the LGN, outlined by the dotted white line, on the qT$_1$ map. (c) Zoomed view of the LGN with an adapted color map to reflect the range of qT$_1$ values within the LGN. Shorter qT$_1$ values closely coincide with the anatomical location of a dorsal P subdivision, whereas longer qT$_1$ values coincide with a ventral M subdivision. (d) LGN qT$_1$ histogram (gray bars), outlined with the obtained Gaussian mixture model fit, as indicated by the gray dashed line. The blue and red curves correspond to the two components in the distribution of qT$_1$ values, that were identified by the Gaussian mixture model. (e) Gaussian P-component, normalized by the envelope of the summed Gaussian components reveals a cluster of short T$_1$ relaxation with high distribution probabilities in dorsal parts of the LGN. (f) Gaussian M-component, normalized by the envelope of the summed Gaussian components reveals a cluster of longer T$_1$ relaxation with high distribution probabilities in ventral parts of the nucleus. (g) Coronal view of the LGN tissue sample, showing the approximate same slice as shown in panels a–c & e, f. Anatomical labels are provided for spatial orientation. LGN = lateral geniculate nucleus, FuG = fusiform gyrus, HC = hippocampus, PHG = parahippocampal gyrus, VPL = ventral posterior lateral thalamic nucleus and other thalamic nuclei. (h) LGN slice, stained for anti-human neuronal protein C/D (anti-HuC/D) for neurons, shows characteristic M and P layering within the LGN. The figure shows the same slice as in panel g and the approximate same slice as in panels a–c & e, f. A typical four-layer LGN segment, consisting of two ventral M layers and two fused dorsal P layers, as often present in posterior parts of the nucleus, is visible (Hickey and Guillery, 1979). M and P subdivisions, outlined in red and blue, respectively, are shown to facilitate visual comparison with qMRI-based subdivision maps. Detailed procedures on the manual tracing and labeling of LGN layers are described in the supplementary materials (SI Methods). (For interpretation of the references to color in this figure legend, the reader is referred to the web version of this article.)

components by the envelope of the summed Gaussian components revealed a cluster of shorter T$_1$ relaxation with high distribution probabilities in dorsal parts of the LGN (Fig. 3e), and a cluster of longer T$_1$ relaxation with high distribution probabilities confined to ventral parts of the nucleus (Fig. 3f). Both clusters coincided with the expected anatomical location of LGN P (shorter T$_1$ relaxation) and M (longer T$_1$ relaxation) subdivisions, respectively. The identified dorsal and ventral subdivision contributed 77.8% and 22.2% to total LGN volume, respectively. This result is well in line with prior histological evidence on subdivisional size distributions in the human LGN of 72–81% for the parvocellular subdivision and 19–28% for the magnocellular subdivision (Andrews et al., 1997).

To validate our results, we compared our *post-mortem* qMRI-based LGN subdivision maps against ground truth microstructural histology on the same LGN tissue sample. Immunohistochemical staining for neurons (anti-HuC/D) of the LGN sample (Fig. 3g, h) revealed a striking resemblence between histologically defined ventral M and dorsal P subdivisions and qT$_1$-based mappings of LGN subdivisions (Fig. 3e, f). A layer-specific stereological analysis of the neuronal cell density within the LGN (Fig. 4a, b) revealed as expected a lower cell density in M than P layers (Andrews et al., 1997; Nassi and Callaway, 2009). A layer-specific optical density analysis of immunohistochemical staining for myelin (anti-MBP) revealed a stronger myelination of the P layers, compared to the M layers in the LGN (Fig. 4c, d). A layer-specific optical
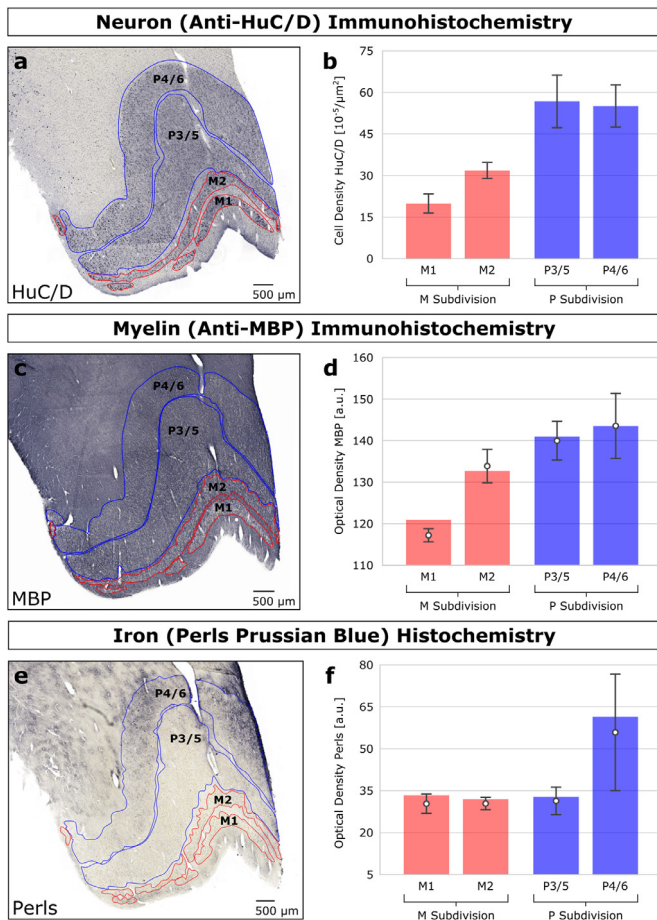
Fig. 4. Histological assessments of microstructural tissue differences between LGN layers. (a) Immunohistochemical staining for neurons (anti-HuC/D) of the LGN specimen. Individual LGN P layers are outlined in blue. LGN M layers are outlined in red. The two layers P4/6 (contralateral input) and P3/5 (ipsilateral input) are fused in this posterior slice of the LGN (same slice as in Fig. 3h). Such fusion of layers is commonly observed in posterior parts of the human LGN (Hickey and Guillery, 1979). (b) Bar graph of stereological assessment of the estimated mean neuronal cell density for individual P (blue) and M (red) layers from data shown in panel a. The mean cell density per layer was approximated through cell counts in $N = 6$ uniformly distributed smaller regions of interest (ROI) in each layer. Error bars indicate ± 1 SD. (c) Immunohistochemical staining for myelin (anti-MBP) of the LGN specimen. LGN P layers are outlined in blue. LGN M layers are outlined in red. The figure shows the approximate same slice as in Figs. 3h and 4a. (d) Bar graph of the MBP optical density of individual P (blue) and M (red) layers from data shown in panel c, in arbitrary units (a.u.). In contrast to the cell density measurements shown in (b), the MBP optical density was extracted for each LGN layer as a whole and thus yielded exactly one value per layer. To provide a measure of the variability within layers, the mean MBP optical density per layer was additionally approximated through optical density measurements in $N = 6$ uniformly distributed smaller ROIs in each layer. The approximated mean MBP optical density per layer is depicted by the white circles and corresponding error bars indicate ± 1 SD. (e) Histochemical staining for ferric iron (Perls' Prussian blue, PB) of the LGN specimen. Individual LGN P layers are outlined in blue. LGN M layers are outlined in red. The figure shows approximately the same slice as in Figs. 3h and 4a, b. (f) Bar graph of the PB optical density of individual P (blue) and M (red) layers from data shown in panel e, in arbitrary units. The PB optical density was extracted for each LGN layer as a whole and thus yielded exactly one value per layer. The mean PB optical density per layer was additionally approximated through optical density measurements in $N = 6$ uniformly distributed smaller ROIs in each layer. The approximated mean PB optical density per layer is depicted by the white circles and corresponding error bars indicate ± 1 SD. (For interpretation of the references to color in this figure legend, the reader is referred to the web version of this article.)

density analysis of histochemical staining for ferric iron (Perls' Prussian blue) yielded no clear distinction in terms of iron content between LGN M and P subdivisions; but interestingly revealed greater iron deposits in the parvocellular segment of fused layers P4/6, which receive visual input from the contralateral eye (Fig. 4e, f).

Taken together, the histological findings show that the P subdivision of the LGN has a higher myelin density than the M subdivision, which could explain the observation of overall shorter T_1 relaxation of the P subdivision than M subdivision on both the *in-vivo* and *post-mortem* qT_1 maps.

4. Discussion

Here, we utilized recent technological advances in qMRI for mapping the human LGN, a key structure in the visual pathway (Saalmann and Kastner, 2011). Using two orthogonal qMRI strategies, we demonstrated that a differentiation of the LGN and its two distinct main subdivisions is possible based on microstructure-informed qMRI contrasts alone. The study overcomes long-standing technical challenges to reveal LGN subdivisions in humans *in-vivo*. It paves the way for imaging subsections of the LGN to obtain a better understanding of its function and microstructure in health and disease.

The quantitative assessment of the LGN and a differentiation of its subdivisions was possible based on qT_1. In both the *in-vivo* and *post-mortem* qMRI data, we were able to identify two components of shorter and longer T_1 relaxation coinciding with the known anatomical locations of dorsal P and ventral M subdivisions, respectively. The observed qT_1 contrast directly related to cyto- and myeloarchitectonic differences between LGN M and P layers. A histological examination of the *post-mortem* LGN sample confirmed a higher cell density in P layers compared to M layers of the LGN (Andrews et al., 1997; Hassler, 1966; Nassi and Callaway, 2009). P layers were further found to have a higher myelin density than M layers. In contrast to cell and myelin density, a comparison of iron content did not yield a clear differentiation between M and P layers. The observed higher myelin density in P than M layers seems at a first glance counter-intuitive, as M axons are known to be more myelinated than P axons (Hassler, 1966; Merigan and Maunsell, 1993; Yoonessi and Yoonessi, 2011). Our findings suggest that the cell density acts as mediating factor for the observed differences in myelin density between P and M layers: the larger amount of less myelinated P axons increases the net myelin density of the P layers of the LGN, as compared to a smaller amount of more heavily myelinated M axons. This implies that although magnocellular axons are *more* myelinated, magnocellular layers contain *less* myelin overall than parvocellular layers and this is reflected in the *in-vivo* and *post-mortem* qT_1 maps. This is novel and could not be directly derived from previous literature (Hassler, 1966; Merigan and Maunsell, 1993; Pistorio et al., 2006; Yoonessi and Yoonessi, 2011). The mediating role of the cell density highlights the crucial need to take cytoarchitectonic tissue features into account when making inferences about myelin density from T_1 relaxometry. An additional contributing factor to the observed subdivisional LGN contrast might be the positive correlation between axon diameter and T_1 relaxation (Does, 2018; Harkins et al., 2016), as M neurons entail larger axons than P neurons (Ichida et al., 2014).

The Gaussian mixture model identified LGN subdivisions on not all of the single-subject *in-vivo* qT_1 maps. However, even in the remaining subjects, a binary thresholding of the LGN qT_1 distributions revealed the same M/P pattern as observed in the model fits. The observed relative size contributions of the successfully identified *in-vivo* and *post-mortem* LGN subdivisions to total LGN volume were well in line with prior histological assessments in the human LGN: 72–81% for the parvocellular subdivision and 19–28% for the magnocellular subdivision (Andrews et al., 1997). The identified *in-vivo* LGN subdivisions showed a large degree of volume variation across participants. This variation might be due to genuine inter-individual differences: the human LGN has an approximately twofold inter-individual variability in vol-

ume (Andrews et al., 1997). This large variation in LGN volume could also extend to large inter-individual differences in M and P subdivision volumes as observed in the present study. Both the large amount of inter-individual variability as well as the number of non-separable *in-vivo* qT_1 distributions could potentially be reduced by further technological improvements. First, there is an inherent trade-off between brain coverage, spatial-temporal resolution and sensitivity in MRI acquisitions (Huber et al., 2020). The image resolution constraints arising from our whole-brain acquisitions were sufficient for *in-vivo* mappings of LGN subdivisions. Custom-tailored *in-vivo* qMRI acquisitions of the LGN with reduced coverage of only a part of the brain for the benefit of increased image resolution are likely to enhance subdivisional LGN contrast even further. Second, multi-modal qMRI approaches, such as multi-parametric mapping (Weiskopf et al., 2014), might further increase microstructural LGN contrast and potentially enable improved LGN subdivision estimations based on multi-dimensional data distributions. Given the increased quantitative contrast, such multi-parametric qMRI data might allow LGN sub-parcellations also at field strengths below 7T. The additional qMRI contrasts might also provide further insight into additional LGN tissue features, such as iron content.

Using qMRI to dissociate between LGN subdivisions offers significant advantages over previous fMRI approaches (Denison et al., 2014; Zhang et al., 2016, 2015). In contrast to fMRI, structural qMRI is (i) characterized by a higher signal-to-noise ratio and allows for acquisitions with higher spatial resolutions; (ii) generally less taxing for participants as no lengthy functional design is required; and (iii) allows to draw conclusions about the underlying microstructure, such as tissue myelination (Stüber et al., 2014).

Besides the findings related to our main aim, we made three further interesting observations. First, while we did not find a clear differentiation in iron content between M and P subdivisions, we did observe greater iron deposits in layers P4/6 (Fig. 4e, f), which receive visual input from the contralateral eye (Hickey and Guillery, 1979). This finding is intriguing as it suggests a different composition of eye-specific contralateral and ipsilateral P layers. In histological preparations, contralateral and ipsilateral P layers show a relatively uniform morphological appearance (Andrews et al., 1997; Hickey and Guillery, 1979), (Figs. 3h, 4a). However, functional differences between contralateral and ipsilateral P layers with respect to response latencies of their constituent neurons have been reported previously in non-human primate research (Maunsell et al., 1999). Whether these functional differences also apply to humans and whether they relate to local differences in iron content is currently unknown. To our knowledge there is no study that has yet examined layer-specific differences in iron content in the human LGN. Iron concentrations in the human brain are known to accumulate with aging (Ramos et al., 2014; Ward et al., 2014). As our LGN sample was obtained from a patient of advanced age (89 years), we cannot exclude the possibility that the elevated iron deposits are due to age-related changes in brain iron concentration levels. However, the specificity of elevated iron deposits in contralateral layers P4/6, and the otherwise low iron content in the thalamus (Rooney et al., 2007; Stüber et al., 2014), make this explanation unlikely.

Second, in light of the elevated iron deposits in LGN layers P4/6, and the inverse relationship between iron content and T_1 relaxation (Stüber et al., 2014), one could have expected an additional qT_1 component centered around the shorter qT_1 range of the identified P component in the *post-mortem* qT_1 LGN distribution. Nonetheless, the *post-mortem* qT_1 LGN distribution bore no sign of an additional qT_1 component that captured the elevated iron deposits in contralateral layers P4/6 (Fig. 3a–d). The lack of such an iron-specific qT_1 component is consistent with the concept that iron content, as compared to myelin density, only has a relatively small contribution to T_1 relaxation (Stüber et al., 2014).

Third, LGN volumes were significantly larger in the right than in the left hemisphere. Indications for larger right-hemispheric LGN volumes in healthy participants have been reported before in MRI (Li et al., 2012;

Papadopoulou et al., 2019) and histological studies (Andrews et al., 1997). Other MRI studies did not find evidence for such lateralization effects (Giraldo-Chica et al., 2015; Mcketton et al., 2014; Müller-Axt et al., 2017). These variable findings might relate to the large inter-individual variability in LGN volume in humans (Andrews et al., 1997); and that previous studies with low or modest sample sizes lack sufficient statistical power to reliably detect potential inter-hemispheric differences in LGN volume (Andrews et al., 1997; Müller-Axt et al., 2017).

The current study paves the way for assessing the function and microstructure of the LGN in humans at unprecedented image resolution. The here presented qMRI-based mapping strategy based on T_1 offers a novel opportunity to discern sub-structures within the human thalamus *in-vivo*. Furthermore, in contrast to conventional non-quantitative MRI, quantitative MR contrasts such as T_1 can be related to microstructure, even within the same tissue type (e.g., within LGN gray matter). This property of qMRI also offers potential applications for sub-parcellations of other subcortical nuclei with distinctive cyto- and myeloarchitectonic tissue features. We expect that our qMRI-based mapping strategy will enable subject-specific analyses of the LGN and its subdivisions. In cases of limited image contrast and/or resolution, we anticipate that our publicly available LGN and M/P subdivision atlases will advance anatomically sound definitions of the LGN and its subsections. For optimal registration quality between lower resolution images and the provided atlases, we recommend using (i) the provided high-resolution qT_1 template as reference image, (ii) subject-specific input images with similar contrast to the reference image (e.g., qT_1 from MP2RAGE), and (iii) advanced nonlinear registration algorithms (e.g., SyN in ANTs). We expect that both our qMRI-based mapping strategy as well as the provided atlases are likely to considerably facilitate research on understanding the LGN's complex role for human perception and cognition. Our proposed strategy will also provide a bridge to two other fields. First, the possibility of imaging subsections of the LGN in humans *in-vivo* can facilitate interactions between human and animal research – such interspecies research is to-date hampered by the different spatial resolutions used in the respective fields. Second, the present study provides a novel opportunity for investigating the contribution of selective impairments in LGN subdivisions to clinical disorders such as multiple sclerosis (Evangelou et al., 2001), glaucoma (Zhang et al., 2016), and developmental dyslexia (Livingstone et al., 1991; Müller-Axt et al., 2017). With high-field MRI systems being more readily available, we are confident that the qMRI contrast demonstrated here will constitute an important milestone for assessing LGN function and dysfunction in humans *in-vivo* both in neuroscientific and clinical settings.

Credit authorship contribution statement

Acknowledgements

and the SPP2041 Priority Program "Computational Connectomics" of the German Research Foundation (DFG).

References

Andrews, T.J., Halpern, S.D., Purves, D., 1997. Correlated size variations in human visual cortex, lateral geniculate nucleus, and optic tract. J. Neurosci. 17, 2859–2868.

Avants, B.B., Epstein, C.L., Grossman, M., Gee, J.C., 2008. Symmetric diffeomorphic image registration with cross-correlation: evaluating automated labeling of elderly and neurodegenerative brain. Med. Image Anal. 12, 26–41.

Avants, B.B., Yushkevich, P., Pluta, J., Minkoff, D., Korczykowski, M., Detre, J., Gee, J.C., 2010. The optimal template effect in hippocampus studies of diseased populations. Neuroimage 49, 2457–2466.

Bazin, P.L., Weiss, M., Dinse, J., Schäfer, A., Trampel, R., Turner, R., 2014. A computational framework for ultra-high resolution cortical segmentation at 7 Tesla. Neuroimage 93, 201–209.

Beaton, A.A., 2004. The Magnocellular Deficit hypothesis. In: Dyslexia, Reading and the Brain: A Sourcebook of Psychological and Biological Research. Psychology Press, Hove, pp. 262–281.

Bernstein, M.A., King, K.F., Zhou, X.J., 2004. Handbook of MRI Pulse Sequences, Handbook of MRI Pulse Sequences. Elsevier Academic Press, Burlington, MA.

Callaway, E.M., 2005. Structure and function of parallel pathways in the primate early visual system. J. Physiol. 566, 13–19.

Denison, R.N., Silver, M.A., 2012. Distinct contributions of the magnocellular and parvocellular visual streams to perceptual selection. J. Cogn. Neurosci. 24, 246–259.

Denison, R.N., Vu, A.T., Yacoub, E., Feinberg, D.A., Silver, M.A., 2014. Functional mapping of the magnocellular and parvocellular subdivisions of human LGN. Neuroimage 102, 358–369.

Dice, L.R., 1945. Measures of the amount of ecologic association between species. Ecology 26, 297–302.

Does, M.D., 2018. Inferring brain tissue composition and microstructure via MR relaxometry. Neuroimage.

Dorph-Petersen, K.A., Caric, D., Saghafi, R., Zhang, W., Sampson, A.R., Lewis, D.A., 2009. Volume and neuron number of the lateral geniculate nucleus in schizophrenia and mood disorders. Acta Neuropathol. 117, 369–384.

Evangelou, N., Konz, D., Esiri, M.M., Smith, S., Palace, J., Matthews, P.M., 2001. Size-selective neuronal changes in the anterior optic pathways suggest a differential susceptibility to injury in multiple sclerosis. Brain 124, 1813–1820.

Forstmann, B.U., de Hollander, G., van Maanen, L., Alkemade, A., Keuken, M.C., 2016. Towards a mechanistic understanding of the human subcortex. Nat. Rev. Neurosci. 18, 57–65.

Geyer, S., Weiss, M., Reimann, K., Lohmann, G., Turner, R., 2011. Microstructural parcellation of the human cerebral cortex - from Brodmann's post-mortem map to *in vivo* mapping with high-field magnetic resonance imaging. Front. Hum. Neurosci. 5, 1–7.

Giraldo-Chica, M., Hegarty, J.P., Schneider, K.A., 2015. Morphological differences in the lateral geniculate nucleus associated with dyslexia. NeuroImage Clin. 7, 830–836.

Gupta, N., Ang, L.C., de Tilly, L.N., Bidaisee, L., Yücel, Y.H., 2006. Human glaucoma and neural degeneration in intracranial optic nerve, lateral geniculate nucleus, and visual cortex. Br. J. Ophthalmol. 90, 674–678.

Harkins, K.D., Xu, J., Dula, A.N., Li, K., Valentine, W.M., Gochberg, D.F., Gore, J.C., Does, M.D., 2016. The microstructural correlates of T1 in white matter. Magn. Reson. Med. 75, 1341–1345.

Hassler, R., 1966. Comparative anatomy of the central visual systems in day-and night-active primates. In: Evolution of the Forebrain. Springer, Boston, MA, pp. 419–434.

Helms, G., Dathe, H., Dechent, P., 2008. Quantitative FLASH MRI at 3T using a rational approximation of the Ernst equation. Magn. Reson. Med. 59, 667–672.

Hickey, T.L., Guillery, R.W., 1979. Variability of laminar patterns in the human lateral geniculate nucleus. J. Comp. Neurol. 183, 221–246.

Huber, L., Finn, E.S., Chai, Y., Goebel, R., Stirnberg, R., Stöcker, T., Marrett, S., Uludag, K., Kim, S.G., Han, S., Bandettini, P.A., Poser, B.A., 2020. Layer-dependent functional connectivity methods. Prog. Neurobiol., 101835.

Ichida, J.M., Mavity-Hudson, J.A., Casagrande, V.A., 2014. Distinct patterns of cortico-geniculate feedback to different layers of the lateral geniculate nucleus. Eye Brain 6, 57–73.

Iglesias, J.E., Crampsie, S., Strand, C., Tachrount, M., Thomas, D.L., Holton, J.L., 2018. Effect of Fluorinert on the histological properties of Formalin-fixed human brain tissue. J. Neuropathol. Exp. Neurol. 12, 1085–1090.

Kuehn, E., Dinse, J., Jakobsen, E., Long, X., Schäfer, A., Bazin, P.L., Villringer, A., Sereno, M.I., Margulies, D.S., 2017. Body topography parcellates human sensory and motor cortex. Cereb. Cortex 27, 3790–3805.

Li, M., He, H., Shi, W., Li, J., Lv, B., Wang, C.H., Miao, Q.W., Wang, Z.C., Wang, N.L., Walter, M., Sabel, B.A., 2012. Quantification of the human lateral geniculate nucleus *in vivo* using MR imaging based on morphometry: volume loss with age. Am. J. Neuroradiol. 33, 915–921.

Livingstone, M., Hubel, D., 1988. Segregation of form, color, movement, and depth: anatomy, physiology, and perception. Science 240, 740–749.

Livingstone, M.S., Rosen, G.D., Drislane, F.W., Galaburda, A.M., 1991. Physiological and anatomical evidence for a magnocellular defect in developmental dyslexia. Proc. Natl. Acad. Sci. U.S.A. 88, 7943–7947.

Lutti, A., Dick, F., Sereno, M.I., Weiskopf, N., 2014. Using high-resolution quantitative mapping of R1 as an index of cortical myelination. Neuroimage 93, 176–188.

Marques, J.P., Gruetter, R., 2013. New developments and applications of the MP2RAGE sequence-focusing the contrast and high spatial resolution R1 mapping. PLoS ONE 8, 1–11.

Marques, J.P., Kober, T., Krueger, G., van der Zwaag, W., Van de Moortele, P.F., Gruetter, R., 2010. MP2RAGE, a self bias-field corrected sequence for improved segmentation and T1-mapping at high field. Neuroimage 49, 1271–1281.

Maunsell, J.H.R., Ghose, G.M., Assad, J.A., Mcadams, C.J., Boudreau, C.E., Noerager, B.D., 1999. Visual response latencies of magnocellular and parvocellular LGN neurons in macaque monkeys. Vis. Neurosci. 16, 1–14.

Mcketton, L., Kelly, K.R., Schneider, K.A., 2014. Abnormal lateral geniculate nucleus and optic chiasm in human albinism. J. Comp. Neurol. 522, 2680–2687.

Merigan, W.H., Maunsell, J.H.R., 1993. How parallel are the primate visual pathways? Annu. Rev. Neurosci. 16, 369–402.

Milne, E., Swettenham, J., Hansen, P., Campbell, R., Jeffries, H., Plaisted, K., 2002. High motion coherence thresholds in children with autism. J. Child Psychol. Psychiatry 43, 255–263.

Müller-Axt, C., Anwander, A., von Kriegstein, K., 2017. Altered structural connectivity of the left visual thalamus in developmental dyslexia. Curr. Biol. 27, 3692–3698.

Müller, R., Lenich, T., Kirilina, E., Möller, H.E., 2019. Application of an RF current mirror for MRI transmit coils. In: Proceedings of the ISMRM 27th Annual Meeting & Exhibition.

Nassi, J.J., Callaway, E.M., 2009. Parallel processing strategies of the primate visual system. Nat. Rev. Neurosci. 10, 360–372.

Oldfield, R.C., 1971. The assessment and analysis of handedness: the Edinburgh inventory. Neuropsychologia 9, 97–113.

Papadopoulou, A., Gaetano, L., Pfister, A., Altermatt, A., Tsagkas, C., Morency, F., Brandt, A.U., Hardmeier, M., Chakravarty, M.M., Descoteaux, M., Kappos, L., Sprenger, T., Magon, S., 2019. Damage of the lateral geniculate nucleus in MS: assessing the missing node of the visual pathway. Neurology 92, 2240–2249.

Pistorio, A.L., Hendry, S.H., Wang, X., 2006. A modified technique for high-resolution staining of myelin. J. Neurosci. Methods 153, 135–146.

Ramos, P., Santos, A., Pinto, N.R., Mendes, R., Magalhães, T., Almeida, A., 2014. Iron levels in the human brain: a post-mortem study of anatomical region differences and age-related changes. J. Trace Elem. Med. Biol. 28, 13–17.

Rooney, W.D., Johnson, G., Li, X., Cohen, E.R., Kim, S.G., Ugurbil, K., Springer, C.S., 2007. Magnetic field and tissue dependencies of human brain longitudinal $1H_2O$ relaxation *in vivo*. Magn. Reson. Med. 57, 308–318.

Saalmann, Y.B., Kastner, S., 2011. Cognitive and perceptual functions of the visual thalamus. Neuron 71, 209–223.

Schneider, K.A., Kastner, S., 2009. Effects of sustained spatial attention in the human lateral geniculate nucleus and superior colliculus. J. Neurosci. 29, 1784–1795.

Shatil, A.S., Uddin, M.N., Matsuda, K.M., Figley, C.R., 2018. Quantitative Ex Vivo MRI changes due to progressive formalin fixation in whole human brain specimens: longitudinal characterization of diffusion, relaxometry, and myelin water fraction measurements at 3T. Front. Med. (Lausanne) 5, 31.

Stein, J., 2002. The neurobiology of reading difficulties. In: Witruk, E., Friederici, A.D., Lachmann, T. (Eds.), Basic Functions of Language, Reading and Reading Disability, Neuropsychology and Cognition. Springer US, Boston, MA, pp. 199–211.

Stein, J., 1997. To see but not to read; the magnocellular theory of dyslexia. Trends Neurosci. 20, 147–152.

Stüber, C., Morawski, M., Schäfer, A., Labadie, C., Wähnert, M., Leuze, C., Streicher, M., Barapatre, N., Reimann, K., Geyer, S., Spemann, D., Turner, R., 2014. Myelin and iron concentration in the human brain: a quantitative study of MRI contrast. Neuroimage 93, 95–106.

Tardif, C.L., Schafer, A., Trampel, R., Villringer, A., Turner, R., Bazin, P.L., 2016. Open Science CBS Neuroimaging Repository: sharing ultra-high-field MR images of the brain. Neuroimage 124, 1143–1148.

Thurtell, M.J., Bala, E., Yaniglos, S.S., Rucker, J.C., Peachey, N.S., Leigh, R.J., 2009. Evaluation of optic neuropathy in multiple sclerosis using low-contrast visual evoked potentials. Neurology 73, 1849–1857.

Tustison, N.J., Avants, B.B., Cook, P.A., Zheng, Y., Egan, A., Yushkevich, P.A., Gee, J.C., 2010. N_4ITK: improved N_3 bias correction. IEEE Trans. Med. Imaging 29, 1310–1320.

van der Zwaag, W., Schäfer, A., Marques, J.P., Turner, R., Trampel, R., 2016. Recent applications of UHF-MRI in the study of human brain function and structure: a review. NMR Biomed. 29, 1274–1288.

Virtanen, P., et al., 2020. SciPy 1.0: fundamental algorithms for scientific computing in Python. Nat. Methods 17, 261–272.

Waehnert, M.D., Dinse, J., Schäfer, A., Geyer, S., Bazin, P.L., Turner, R., Tardif, C.L., 2016. A subject-specific framework for *in vivo* myeloarchitectonic analysis using high resolution quantitative MRI. Neuroimage 125, 94–107.

Ward, R.J., Zucca, F.A., Duyn, J.H., Crichton, R.R., Zecca, L., 2014. The role of iron in brain ageing and neurodegenerative disorders. Lancet Neurol. 13, 1045–1060.

Weibull, A., Gustavsson, H., Mattsson, S., Svensson, J., 2008. Investigation of spatial resolution, partial volume effects and smoothing in functional MRI using artificial 3D time series. Neuroimage 41, 346–353.

Weiskopf, N., Callaghan, M.F., Josephs, O., Lutti, A., Mohammadi, S., 2014. Estimating the apparent transverse relaxation time (R2*) from images with different contrasts (ESTATICS) reduces motion artifacts. Front. Neurosci. 8, 1–10.

Yoonessi, Ali, Yoonessi, Ahmad, 2011. Functional assessment of magno, parvo and konio–cellular pathways; current state and future clinical applications. J. Ophthalmic Vis. Res. 6, 119–126.

Yücel, Y.H., Zhang, Q., Weinreb, R.N., Kaufman, P.L., Gupta, N., 2003. Effects of retinal ganglion cell loss on magno-, parvo-, koniocellular pathways in the lateral geniculate nucleus and visual cortex in glaucoma. Prog. Retin. Eye Res. 22, 465–481.

Zhang, P., Wen, W., Sun, X., He, S., 2016. Selective reduction of fMRI responses to transient achromatic stimuli in the magnocellular layers of the LGN and the superficial layer of the SC of early glaucoma patients. Hum. Brain Mapp. 37, 558–569.

Zhang, P., Zhou, H., Wen, W., He, S., 2015. Layer-specific response properties of the human lateral geniculate nucleus and superior colliculus. Neuroimage 111, 159–166.